First-principles studies on the electronic and mechanical properties of two-dimensional (2D) materials

NG YI SHENG

A project report submitted in partial fulfilment of the requirements for the award of Bachelor of Science (Honours) Physics

Lee Kong Chian Faculty of Engineering and Science
Universiti Tunku Abdul Rahman

September 2020

DECLARATION

I hereby declare that this project report is based on my original work except for citations and quotations which have been duly acknowledged. I also declare that it has not been previously and concurrently submitted for any other degree or award at UTAR or other institutions.

Signature   :

Name   :   Ng Yi Sheng

ID No.   :   1800080

Date   :   14/9/2020

APPROVAL FOR SUBMISSION

I certify that this project report entitled **"First-principles studies on the electronic and mechanical properties of two-dimensional (2D) materials"** was prepared by **NG YI SHENG** has met the required standard for submission in partial fulfilment of the requirements for the award of Bachelor of Science (Honours) Physics at Universiti Tunku Abdul Rahman.

Approved by,

Signature   :

Supervisor   :   Dr. Yeoh Keat Hoe

Date   :   14/9/2020

The copyright of this report belongs to the author under the terms of the copyright Act 1987 as qualified by Intellectual Property Policy of Universiti Tunku Abdul Rahman. Due acknowledgement shall always be made of the use of any material contained in, or derived from, this report.

ACKNOWLEDGEMENTS

ABSTRACT

Since the discovery of Graphene, two-dimensional (2D) material or monolayer has been attracting huge interest. By stacking two different monolayers on top of one another, we can obtain heterostructure, which has different physical properties compared with the individual monolayers. In this work, using the first-principles method within the Density Functional Theory (DFT) framework, we have discovered a new stable heterostructure by stacking monolayer Ge (Germanene) and monolayer SiGe (Siligene). The new heterostructure is stable as evidenced by the lack of negative frequency in the phonon dispersion, and exhibits metallic characteristic as indicated by the presence of electronic states at the Fermi level. Under more than 6% tensile strain or 4% compressive strain, the heterostructure starts to fracture mechanically with ultimate tensile strength of about 18 GPa. Besides, the metallic characteristic of the heterostructure shifts from metallic to semimetallic under 6% biaxial tensile strain. When oxygen atoms are adsorbed onto the surface of the heterostructure, a band gap of 0.24 eV is induced. The metallic heterostructure may be applicable for future development of nano scale battery anode or IC interconnects.

TABLE OF CONTENTS

LIST OF TABLES

LIST OF FIGURES

LIST OF SYMBOLS / ABBREVIATIONS

2D	Two Dimensional
TMD	Transition Metal Dichalcogenides
DFT	Density Functional Theory
DFPT	Density Functional Perturbation Theory
SCF	Self-Consistent Field
LDA	Local Density Approximation
GGA	Generalized Gradient Approximation
PBE	Perdew-Burke-Ernzerhof
PAW	Projected Augmented Wave
XC	Exchange-Correlation
DOS	Density of States
PDOS	Partial Density of States
BZ	Brillouin Zone
LB	Low-Buckled
QE	Quantum ESPRESSO
Å	Angstrom, 10^{-10} meter
Ry	Rydberg, 13.6 eV
eV	Electron-volt
E_F	Fermi Level
E	Energy
Si	Silicon
Ge	Germanium
SiGe	Silicon-Germanium
MoS_2	Molybdenum Disulphide
O	Oxygen
i	Imaginary Number
$\hbar$	Reduced Planck Constant
m	Electron Mass
$\rho(\boldsymbol{r})$	Electron Charge Density at Point $\boldsymbol{r}$
$\hat{H}$	Hamiltonian Operator
∇^2	Laplacian Operator

ϕ_i	i^{th} non-interacting orbital
ψ	Wavefunction
δ_{mn}	Kronecker Delta
$E[\rho]$	Energy Functional
V_{ext}	External Potential
T	Kinetic Energy
E_0	Ground State Energy
V_H	Hartree Energy
E_{XC}	Exchange-Correlation Energy
H_{KS}	Kohn-Sham Hamiltonian
det	Determinant

CHAPTER 1

INTRODUCTION

1.1   Introduction to 2D Materials

2D materials or two-dimensional materials refer to a family of material which consists of substances made up of a layer of atoms, which are also known as monolayer. An example of 2D material is shown in Figure 1.1.
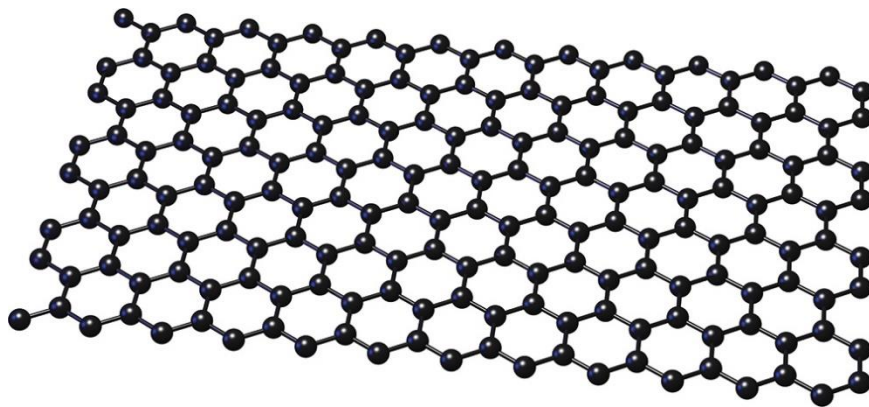
Figure 1.1: Atomic Structure of Graphene, a 2D Material (Graphene, n.d.)

2D materials first debuted on the stage of material science with the successful synthesis of Graphene in 2004, a 2D allotrope of carbon (Novoselov, 2004). Graphene was dubbed 'miracle material' as it possesses many exotic properties such as a very high electron mobility of 15 000 cm^2/Vs (compared to bulk Silicon with 1400 cm^2/Vs) and high tensile strength (Novoselov *et al*., 2012). Even though Graphene has seen a lot of optoelectronic applications, it has limitations on its application to electronics due to the absence of a bandgap which limits the ability for graphene to switch off (Liu *et al*., 2013). Since then, other 2D materials have been continuously discovered and predicted, such as hexagonal boron nitrides, silicene, transition metal dichalcogenides (TMD), MXenes, and perovskite (Zhang, Chhowalla and Liu, 2018). More recently, 2D Pcnitogens (Group V elements) have been studied, such as monolayer phosphorus (Li *et al*., 2014). 2D materials have attracted a considerable amount of attention because of their novel properties, with graphene as the prime example (Butler *et al.*, 2013).

Many bulk materials are actually made up of stacked monolayers that have weak van der Waals bonding between the layers, which allow them to be exfoliated mechanically (Novoselov *et al.*, 2005). 2D materials are also better at withstanding larger strain compared to their bulk counterparts (Dai, Liu and Zhang, 2019), and exhibit different properties, such as having a direct band gap compared to its bulk having an indirect band gap (Song, Hu and Zeng, 2013). The ultrathin 2D material can also be bent or folded easily (Zhang, Akatyeva and Dumitrica, 2011), which allows the 2D material to be applied in origami (Zhu and Li, 2014). Biomedical applications are also feasible because of its flexibility and stretchability, while still having equal or better electronic conductivity than metal and silicon (Akinwande *et al*., 2017), in which graphene has seen applications as electrodes for simultaneous electrophysiology and neuroimaging (Kuzum *et al*., 2014).

The electronic and optical properties of 2D materials can also be tuned by straining the material, which can change the band gap, or shift the band gap from indirect to direct (Roldán *et al*., 2015). Atoms or molecules can be adsorbed onto the surface of 2D materials, changing their band structure, density of states, and charge density (Garay-Tapia, Romero and Barone, 2012).

1.2   Introduction to Heterostructure

Heterostructures are structures that are made by stacking two or more identical or different monolayers on top of each other. They are also known as Van der Waals' heterostructures as they are supported by Van der Waals' forces which act between the monolayer, holding them together (Geim and Grigorieva, 2013).

Heterostructure was first explored experimentally by (Ponomarenko *et al.,* 2011). They stacked two graphene layers together and sandwiched them between two boron nitrides. The heterostructure showed Anderson localization, which is not observed on single-layer graphene. Thus, they have shown that heterostructure can have properties that are very different from its constituent monolayers, which has sparked huge interest in the research of heterostructures.

1.3   Problem Statement

The search for a material that has high charge carrier mobility and a sizable band gap is important for nanoelectronics application as a high-performance field-

effect transistor (Quhe *et al.,* 2012). According to Akinwande *et al.* (2019), the quest has becoming more pressing as the Moore's law is coming to an end as the downscaling of field-effect transistor made from bulk semiconductor is limited by issues such as short-channel effect. The introduction of FinFETs temporarily solved the issue, but they are also limited by the size and the numbers of fins, which again is linked to similar limitations. Hence, slim channel materials that have high charge carrier mobility are highly sought after to overcome this issue. As mentioned in Section 1.1, graphene is unfortunately unable to solve the issue posed as graphene does not have a band gap despite its other significant electronic properties.

Since the synthesis of graphene, many other different monolayers have been explored, with some of them such as monolayer MoS_2 having great promise for application in nanoelectronics (Akbari *et al.,* 2018). However, the search for more materials should be continued as there is always a possibility that an exotic material is waiting to be discovered.

1.4   Aim and Objectives

This final year project aims to predict a new heterostructure based on monolayer Ge (germanene) and monolayer SiGe (siligene) and study the mechanical and electronic properties of this new heterostructure using the first-principle method within the density functional theory (DFT) framework. To reach this final goal, four objectives need to be completed.

The first objective is to study and conduct a literature review for the monolayers involved in the heterostructure, which are germanene and siligene. Literature review is important to allow us to understand the properties of the monolayers, which will aid us in predicting and understanding the properties of the heterostructure at the end of our research. By simulating the monolayers, we can compare the obtained results with published literature to verify whether the parameters used are appropriate.

The second objective is to study the structural and mechanical properties of the heterostructure such as the structural parameters, phonon dispersion, and stress-strain response. From the structural parameters, we can determine the structure of the heterostructure, whereas the phonon dispersion of the heterostructures, which is computed using density functional perturbation

theory (DFPT), is important to determine the feasibility of synthesising the structure experimentally. Understanding the stress-strain response of the heterostructure will allow us to understand how much strain can the heterostructure handle before breaking down, and from there, we can know the maximum strain that we can apply to the heterostructure to tune its electronic properties.

The third objective is to investigate the electronic properties of the heterostructure. This can be done by calculating and plotting the electronic band structure. From there, we can determine the type of the material, whether it is a semiconductor, metal, or semimetal. We can also plot the density of states to further confirm its characteristics.

The fourth objective is to probe the tunability of the heterostructure. By applying strain or adsorbing atoms onto the surface of the heterostructure, the electronic properties can be tuned, which can extend the applicability of the heterostructure and attracts more interest.

1.5   Scope and Limitation of the Study

The scope of this study is to provide us information on the feasibility of the Germanene-Siligene structure and their structural, mechanical, and electronic properties, as well as tunability of the electronic properties by implementing the Density Functional Theory with the Gradient Generalized Approximation (GGA) functional. Structural properties investigated include the lattice constant, buckling distance, phonon dispersion; mechanical properties include the stress-strain curve; electronic properties include electronic band structure and density of states. The tunability of electronic properties will be studied by applying biaxial tensile and compressive strain on the heterostructure, and oxygen adsorption.

One of the limitations faced is the limited computational resource. The calculation of our heterostructure is limited to a 1×1 supercell, which only consists of 1 repeating unit of our structure. If a larger supercell is possible, we can consider investigating the effect of transition metal intercalation, which are better done with a larger (3×3 or 4×4) supercell. Furthermore, the k points grid used in this experiment is $25 \times 25 \times 1$, which is adequate, but a denser grid would increase the accuracy of the results.

Another limitation is the limited duration of this project, which is restricted to 8 months. The phonon dispersion calculation takes up to 2-3 months to complete. Any error made in setting up the calculation would require a restart of the calculation that is already running for some time, thus wasting the precious time allocated. Sometimes, the phonon dispersion may require a denser q point grid to avoid numerical error caused by approximation or interpolation. Denser q mesh would possibly require an addition of several months to the computational time. Hence, we must choose a smaller q mesh to complete the project in the given time.

CHAPTER 2

THEORETICAL BACKGROUND

2.1 Quantum Mechanics Preliminaries

Schrödinger's Equation is a partial differential equation which takes the form

$$i\hbar \frac{\partial \Psi(\vec{r},t)}{\partial t} = \widehat{H}\Psi(\vec{r},t) \tag{2.1}$$

where i is imaginary number, $\hbar$ is the Planck's constant, $\widehat{H}$ is the Hamiltonian, and $\Psi(\vec{r},t)$ is the wavefunction. Hamiltonian is system-specific, but the general form is

$$\widehat{H} = -\frac{\hbar^2}{2m}\nabla^2 + V(\vec{r},t) \tag{2.2}$$

where m is the mass of the particle examined, ∇^2 is the Laplacian, and V is the potential function of the system.

For a system consisting of time-independent potential, we can allow the wavefunction to be separable, i.e. $\Psi(\vec{r},t) = \psi(\vec{r})f(t)$, which allows the Schrödinger's Equation to be split into two differential equation, with both equal to a constant, which is assigned as E_n.

$$i\hbar \frac{\partial f(t)}{\partial t} = E_n f(t) \tag{2.3}$$

$$\widehat{H}\psi(\vec{r}) = E_n \psi(\vec{r}) \tag{2.4}$$

Equation 2.3 is easily solved, with solution $f(t) = e^{-\frac{iE_n t}{\hbar}}$. Equation 2.4 is an eigenvalue equation and is system dependent. The eigenvalue equation can have infinitely many solutions, which are known as eigenstates, ψ_n, and each of them has an eigenvalue, E_n, assigned to them, which may or may not be degenerate. The eigenvalue is the energy of the system in a particular eigenstate, and they can be arranged in ascending order i.e., $E_0 \leq E_1 \leq \cdots < E_n \leq E_{n+1} \ldots < \cdots$

such that there is a minimum value, E_0 which is known as the ground state energy. The full set of eigenstates forms a complete basis in the function space, and any arbitrary wavefunction can be expressed in terms of the superposition of the eigenstates.

2.1.1   Variational Principle

In Quantum Mechanics, there are many different systems which can be either impossible or required too much work to solve. Fortunately, we can exploit the completeness of eigenstates to obtain information about the system such as the ground state energy without actually solving the differential equation. As stated in the previous section, any arbitrary wavefunction, $\phi(\vec{r})$, within the provided constraint, can be written in terms of the superposition of the eigenstates, i.e. a Fourier series:

$$\phi(\vec{r}) = \sum_{n=0}^{\infty} c_n \psi_n \tag{2.5}$$

The expectation value of energy can be written as a functional (the positional dependence is omitted for brevity).

$$E[\phi] = \frac{\int \phi^* \hat{H} \phi \, d^3\vec{r}}{\int \phi^* \phi \, d^3\vec{r}} \tag{2.6}$$

Combining Equation 2.5 and 2.6,

$$E[\phi] = \frac{\sum_{n,m=0}^{\infty} c_n c_m^* \int \psi_m^* \hat{H} \psi_n \, d^3\vec{r}}{\sum_{n,m=0}^{\infty} c_n c_m^* \int \psi_m^* \psi_n \, d^3\vec{r}} \tag{2.7}$$

Using Equation 2.4,

$$E[\phi] = \frac{\sum_{n,m=0}^{\infty} c_n c_m^* E_n \int \psi_m^* \psi_n \, d^3\vec{r}}{\sum_{n,m=0}^{\infty} c_n c_m^* \int \psi_m^* \psi_n \, d^3\vec{r}} \tag{2.8}$$

Since the eigenstates can be made to be orthonormal by using Gram-Schmidt orthonormal process, such that $\int \psi_m^* \psi_n \, d^3\vec{r} = \delta_{mn}$, the expression can be simplified to

$$E[\phi] = \frac{\sum_{n=0}^{\infty} |c_n|^2 E_n}{\sum_{n=0}^{\infty} |c_n|^2} \tag{2.9}$$

With this equation, we can establish an inequality:

$$E[\phi] = \frac{\sum_{n=0}^{\infty} |c_n|^2 E_n}{\sum_{n=0}^{\infty} |c_n|^2} \geq \frac{E_0 \sum_{n=0}^{\infty} |c_n|^2}{\sum_{n=0}^{\infty} |c_n|^2} = E_0 \tag{2.10}$$

which states that any arbitrary trial wavefunction has energy higher or equal to the ground state energy. The true ground state energy can be approached by refining the guess of trial wavefunction iteratively.

2.1.2 Identical Particles

In quantum mechanics, elementary particles of the same type occupying space close to each other must be regarded as identical and lose their distinguishability, such that their collective wavefunction cannot be written as

$$\psi(r_1, r_2, \dots, r_N) = \Pi_i^N \chi_i(r_i) \tag{2.11}$$

where χ_i represent the individual wavefunction for the ith particle. Instead, the wavefunction should be expressed as the superposition of the individual wavefunctions with all of the different possible combinations between the individual wavefunctions and the position labels $(r_1, r_2, ..)$ exhausted. Two different superpositions are possible depending on the type of the elementary particles involved, which are boson and fermion. Since protons and electrons are fermions, we will only include the discussion for fermion.

Fermions, upon exchanging one pair of position labels, i.e. $r_1 \leftrightarrow r_2$, the wavefunction is asymmetric and changes its sign, $\psi \rightarrow -\psi$. The collective wavefunction of a system of identical fermions can be expressed concisely using Slater's determinant:

$$\psi(r_1, r_2, \dots, r_n) = \frac{1}{\sqrt{N!}} \begin{vmatrix} \chi_1(r_1) & \chi_2(r_1) & \cdots & \chi_N(r_1) \\ \chi_1(r_2) & \chi_2(r_2) & \cdots & \chi_N(r_2) \\ \vdots & \vdots & \ddots & \vdots \\ \chi_1(r_N) & \chi_2(r_N) & \cdots & \chi_N(r_N) \end{vmatrix} \tag{2.12}$$

2.1.3 Hellmann-Feynman theorem

Hellman-Feynman theorem states:

$$\frac{dE_\lambda}{d\lambda} = \int \psi_\lambda^* \frac{d\widehat{H}_\lambda}{d\lambda} \psi_\lambda dr \tag{2.13}$$

or more elegantly in Dirac bra-ket notation:

$$\frac{dE_\lambda}{d\lambda} = \left\langle \psi_\lambda \left| \frac{d\widehat{H}_\lambda}{d\lambda} \right| \psi_\lambda \right\rangle \tag{2.14}$$

This theorem is applied in condensed matter physics to compute the atomic forces acting on nuclei of the system. The expression for such force on the jth nucleus is (where $\{\vec{R}\}$ implies the set of vectors $\vec{R_1}, \vec{R_2}, \dots, \vec{R_n}$):

$$\vec{F}_j = -\frac{\partial E\{\vec{R}\}}{\partial \vec{R_1}} = \left\langle \psi_{\{\vec{R}\}} \left| \frac{d\hat{H}_{\{\vec{R}\}}}{d\vec{R_j}} \right| \psi_{\{\vec{R}\}} \right\rangle \tag{2.15}$$

2.2   Density Functional Theory (DFT)

In any material, there are many protons and electrons, and each of them create a Coulomb's potential around them. In the study of condensed matter physics, we are required to take into account the motions and interactions of every single particle in the system. The Hamiltonian of such many-body system is given as (boldface indicates vector):

$$\hat{H}(\boldsymbol{R},\boldsymbol{r}) = -\overbrace{\sum_i \frac{\hbar^2}{2m}\nabla_r^2}^{\substack{\text{Kinetic energy} \\ \text{of electrons}}} - \overbrace{\sum_N \frac{\hbar^2}{2m}\nabla_R^2}^{\substack{\text{Kinetic energy} \\ \text{of protons}}} + \overbrace{\frac{1}{2}\sum_{i \neq j} \frac{e^2}{|r_i - r_j|}}^{\substack{\text{Coulomb interaction} \\ \text{between electrons}}} - \overbrace{\sum_{N,i} \frac{Z_N e^2}{|R_N - r_i|}}^{\substack{\text{Coulomb interaction} \\ \text{between electrons and} \\ \text{protons}}}$$
$$+ \underbrace{\frac{1}{2}\sum_{N,N'} \frac{Z_N Z_{N'} e^2}{|R_N - R_{N'}|}}_{\substack{\text{Coulomb interaction} \\ \text{between protons}}} \tag{2.16}$$

To reduce the complexity of the task, Born-Oppenheimer (BO) approximation is applied, which removes two terms in the Hamiltonian by assuming that the protons are static on the basis that they are much heavier than the electrons. The resultant BO Hamiltonian is thus much cleaner:

$$\hat{H}_{BO}(\boldsymbol{R},\boldsymbol{r}) = -\sum_i \frac{\hbar^2}{2m}\nabla_r^2 + \frac{1}{2}\sum_{i \neq j} \frac{e^2}{|r_i - r_j|} - \sum_{N,i} \frac{Z_N e^2}{|R_N - r_i|} \tag{2.18}$$

In the 1960s, Walter Kohn and Pierre Hohenberg derived two theorems which laid the fundamental of DFT. The first theorem states that the external

potential (Coulomb interaction between the protons and electrons) and subsequently the BO Hamiltonian is a unique functional of electron density, which is denoted by $\rho(\boldsymbol{r})$ (Harrison, 2003):

$$E[\rho] = F[\rho(\boldsymbol{r})] + V_{ext}[\rho] \tag{2.19}$$

where $V_{ext}[\rho(\boldsymbol{r})]$ is the external potential functional

$$V_{ext}[\rho] = -\int \sum_{N,i} \frac{Z_N e^2}{|\boldsymbol{R}_N - \boldsymbol{r}_i|} \rho(\boldsymbol{r}) \, d\boldsymbol{r} \tag{2.20}$$

and $F[\rho(\boldsymbol{r})]$ is the other functional which are still unknown, as the theorem does not provide us. However, we can split it further based on our knowledge of the Hamiltonian:

$$F[\rho] = T[\rho] + V_{ee}[\rho] \tag{2.21}$$

where the first term on the right-hand side is the kinetic energy functional and the second term is the electron-electron Coulomb interaction functional.

The 2nd Kohn-Hohenberg theorem then states that for any trial electron density that satisfies the integral

$$\int \rho_t(\boldsymbol{r})d\boldsymbol{r} = n \tag{2.22}$$

which n is the total number of electrons, then the functional stated in Equation 2.19 becomes

$$E[\rho_t] \geq E_0 \tag{2.23}$$

which we know to be true from the variational principle with the Hamiltonian determined by trial wavefunction.

The two theorems above combined yield the fundamental statement of DFT (Harrison, 2003):

$$\delta\big[E[\rho] - \mu\big(\textstyle\int \rho(\boldsymbol{r})d\boldsymbol{r} - N\big)\big] = 0 \qquad (2.24)$$

which is a Lagrange multiplier with constraint μ. The equation states that the true ground state electron density minimises the functional $E[\rho]$ and gives the true ground state energy when acted on by the functional.

The fundamental statement of DFT has merely stated that the true ground state electron density minimizes the energy functional without providing any direction to obtain the functional.

Kohn then worked with Lu Jeu Sham and they suggested the use of non-interacting electron orbitals to construct anti-symmetric wavefunction with Slater's determinant (Kohanoff, 2006):

$$\Phi = \det[\phi_1 \phi_2 \dots \phi_n] \qquad (2.25)$$

where ϕ_i, $i = 1,2,3,\dots,n$, are the non-interacting electron orbitals of the system. Then, we can construct electron density:

$$\rho(\boldsymbol{r}) = \sum_{i=1}^{n} |\phi_i|^2 \qquad (2.26)$$

By doing so, the non-interacting kinetic energy functional can be constructed:

$$T_s[\rho] = -\frac{\hbar^2}{2m}\sum_{i=1}^{n}\int \phi_i^* \nabla^2 \phi_i \, d\boldsymbol{r} \qquad (2.27)$$

where the subscript s denotes that it is not exact. Because the electrons are assumed to be non-interacting, and they would attain different value otherwise.

They then took the Hartree energy term from Hartree-Fock method as the electron-electron Coulomb interaction functional, which can be explicitly written as (Harrison, 2003):

$$V_H[\rho] = \frac{e^2}{2} \int \frac{\rho_1(\boldsymbol{r_1})\rho_2(\boldsymbol{r_2})}{|\boldsymbol{r_1} - \boldsymbol{r_2}|} d\boldsymbol{r_1} d\boldsymbol{r_2} \qquad (2.28)$$

Note that the energy functional no longer takes the form of Eqn. 2.19, the new energy functional is:

$$E[\rho] = T_s[\rho] + V_{ext}[\rho] + V_H[\rho] + E_{XC}[\rho] \qquad (2.29)$$

From the Eqn. 2.29 above, we can see that a new functional $E_{XC}[\rho]$ has been introduced. The new functional is known as exchange-correlation (XC) functional and is introduced to take into account the error made by assuming the electrons are non-interacting:

$$E_{XC}[\rho] = (T[\rho] - T_s[\rho]) + (V_{ee}[\rho] - V_H[\rho]) \qquad (2.30)$$

After we substitute the electron density (Eqn. 2.24) into the energy functional (Eqn. 2.28), we plug the result into the fundamental statement of DFT (Eqn. 2.22), we arrive at what is known as Kohn-Sham (KS) equation:

$$\left[-\frac{\hbar^2}{2m} \nabla^2 + V_{ext}(\boldsymbol{r}) + V_H(\boldsymbol{r}) + V_{XC}(\boldsymbol{r}) \right] \phi_i(\boldsymbol{r}) = \varepsilon_i \phi_i(\boldsymbol{r}) \qquad (2.31)$$

which is the Schrödinger's equation for the non-interacting one-electron orbital, where we can further define the KS Hamiltonian to be:

$$H_{KS} = \left[-\frac{\hbar^2}{2m} \nabla^2 + V_{ext}(\boldsymbol{r}) + V_H(\boldsymbol{r}) + V_{XC}(\boldsymbol{r}) \right] \qquad (2.32)$$

where, V_{XC}, is the XC potential, defined as the functional derivative of the XC functional,

$$V_{XC}(\boldsymbol{r}) = \frac{\delta E_{XC}(\boldsymbol{r})}{\delta \rho(\boldsymbol{r})} \qquad (2.33)$$

The exact form of XC functional remains unknown. Fortunately, efforts to approximate the functional has been thus far successful using empirical data and Monte-Carlo method, which will be further discussed in the next section.

KS equation can be solved by diagonalizing the KS Hamiltonian, which allows us to obtain the full set of orbitals, and from there, we can construct the updated electron density. The whole problem is solved iteratively by using a multistep process known as self-consistent field (SCF) calculation, which can be summarized in the flow chart shown in Figure 2.1.

After convergence has been achieved for SCF calculation, forces can be calculated using Hellmann-Feynman force (Eqn. 2.15), whereas the energy of the system can be calculated by substituting the final electron density into the energy functional (Eqn. 2.29).
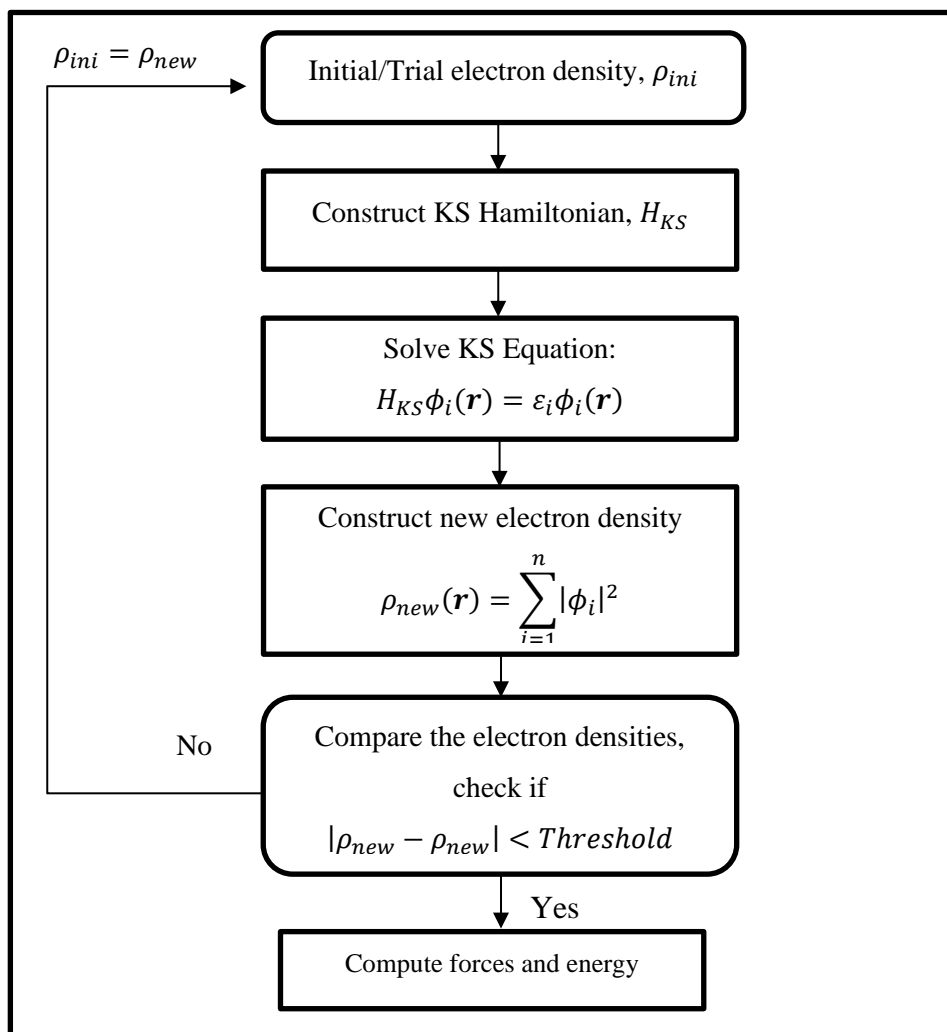
Figure 2.1: Self-Consistent Field (SCF) Calculation Loop Flow Chart

2.2.1 Exchange-Correlation (XC) Functional

Exchange-Correlation functional, E_{XC} is the last missing piece in this DFT scheme discussion. The research field for this functional is currently very active, and many different approximations have been implemented, such as Local Density Approximation (LDA), Generalized Gradient Approximation (GGA), meta-GGA, and Hybrid Functional. The computational resources required is typically in this ascending order: LDA, GGA, meta-GGA, Hybrid, due to the factors that the functionals take into account. However, more sophisticated functional does not always give better result, and the improvement of using complicated functional may be outweighed by the increase of computational cost.

Generalized Gradient Approximation is the functional used in this project. It considers the local electron density, ρ, and the first-order gradient term, $\nabla^2 \rho$, whereas LDA only consider the local electron density, hence it is known as 'local density' approximation. According to Harrison (2003), the typical form of GGA functional is:

$$E_{XC} = \int \rho(\boldsymbol{r}) \varepsilon_{XC}[\rho(\boldsymbol{r}), \nabla \rho(\boldsymbol{r})] d\boldsymbol{r} \qquad (2.34)$$

where $\varepsilon_{XC}[\rho(\boldsymbol{r}), \nabla \rho(\boldsymbol{r})]$ is a semilocal function which has many different variations, which include BLYP, PW91, PBE, and others. In this project, the Perdew-Burke-Ernzerhof Generalized Gradient Approximation (PBE-GGA) functional is utilized.

2.2.2 Pseudopotential

Pseudopotential is an approximation method which freezes the core or non-valence electrons which are highly localized and does not involve in chemical reaction. They are replaced with a smooth density while keeping the important physical characteristics of the core electrons (Sholl and Stecker, 2009). This method significantly reduces the number of electrons involves in the computation, which subsequently reduces the computation time. There are 3 main types of pseudopotentials, which are norm-conserving, ultrasoft, and plane-augmented wave (PAW).

CHAPTER 3

LITERATURE REVIEW

3.1   Germanene

Germanium belongs to the same group as carbon in the periodic table, which is Group 14. In 1994, Takeda and Shiraishi predicted the possibility of germanium monolayer, which is further confirmed 15 years later by Cahangirov *et al.* (2009).

3.1.1   Structural Properties

By calculating and plotting the phonon dispersion (see Figure 3.1(b)), Cahangirov *et al.* (2009) showed that the low-buckled (LB) honeycomb structure (shown in Figure 3.1(a)) is stable for Germanene, in agreement with what Takeda and Shirashi (1994) had predicted. They also considered the possibility of planar and high-buckled structures, but they are shown to be unstable as they have large imaginary frequencies in the Brillouin Zone. The LB honeycomb structure was further confirmed by using *Ab-initio* molecular dynamics at 800 K with time steps of 2 femtoseconds for 10 picoseconds which the structure remained intact. Germanene has been successfully synthesized experimentally in 2014 (Dávila *et al.,* 2014), proving its experimental feasibility.

Structural constants i.e. lattice constant and buckling distance from different sources are tabulated in Table 3.1. From the table, we can see that the reported value for lattice constant from different sources are very close to each other, with at most a difference of 0.156 Å or 4% difference.
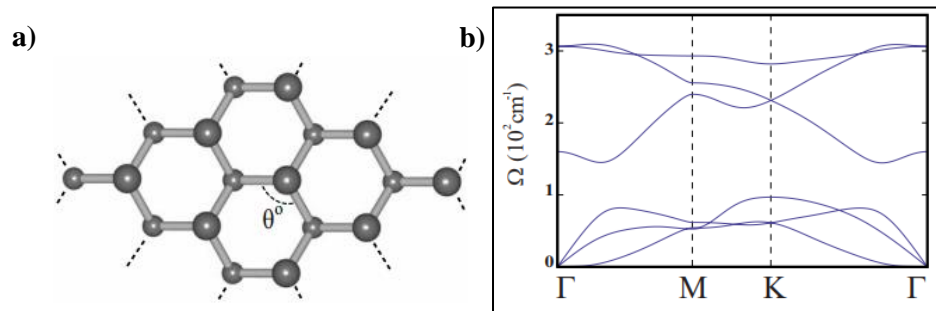
Figure 3.1: (a) Top view and (b) Phonon Dispersion for LB Germanene (Şahin *et al.*, 2009)

Table 3.1: Structural Constants of Germanene from Multiple Sources

Sources	XC Functional	Lattice Constant, Å	Buckling Distance, Å
Cahangirov *et al.* (2009)	LDA	3.97	0.64
Lebègue and Eriksson (2009)	LDA	4.034	(Not included)
	GGA	4.126	(Not included)
Ni *et al.* (2012)	GGA	4.063	0.676
Houssa *et al.* (2010)	LDA	4.03	(Not included)
Yan *et al.* (2015)	LDA	3.95	0.64

3.1.2   Electronic Properties and Tunability

By calculating and plotting the electronic band structure (shown in Figure 3.2), Cahangirov *et al.* (2009) stated that Germanene is semimetallic with a linear crossing point at the K point of the Brillouin Zone (BZ), which indicates the charge carriers behave like massless Dirac fermion. They also stated the band structure around K point is symmetrical, which has attributed the ambipolar properties to Germanene. The results of Houssa *et al.* (2010) agree with Cahangirov *et al*. (2009).

In chapter 1, we mentioned that the vertical electric field and strain can be applied to possibly tune the band structure or change the band gap. The effect of vertical electric field was first investigated in 2012 by Ni *et al.*, which reported a linear relation between band gap opening and electric field. At electric field strength of 1 V/Å, the band gap of Germanene is opened to about 0.1 eV, which is larger than the thermal energy of about 0.026 eV at room temperature. They also noted that since the GGA functional underestimates band gap, the real band gap opening should be much greater than the value calculated. This properties of Germanene allows it to be applied in nanoelectronics, especially as field-effect transistor.

The effect of biaxial strain on the electronic properties of germanene was investigated by Yan *et al*. (2015). They reported a movement of conduction band maximum (CBM) to Fermi level at Γ point of the BZ when 3% biaxial tensile strain is applied to Germanene. The CBM sinks further below the Fermi level when 5% strain is applied. The findings imply that the Germanene

undergoes a transition from semimetal to metal when 3% or more biaxial strain is applied.

When biaxial compressive strain is applied, there are no notable changes reported by Yan *et al.* (2015), with only a shift of the CBM at Γ point further away from the Fermi level. They further investigated the stability of the strained germanene by plotting the phonon dispersion. The phonon dispersion shows small negative modes, but the authors remarked that it was caused by the interpolation error, which can be corrected by increasing the density of q grid.
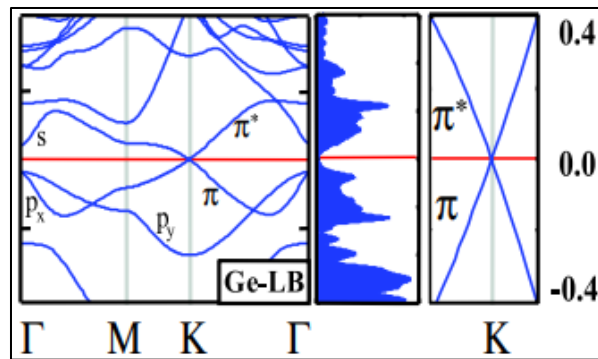
Figure 3.2: (Left to Right) Electronic Band Structure, Density of States, and Zoomed-in View of Electronic Band Structure at K Point Showing Dirac Point for LB Germanene. (Cahangirov *et al.*, 2009)

3.2   Siligene

Siligene or monolayer SiGe was first studied by Pan *et al.,* (2011) along with other group IV monolayers using DFT. Siligene was then investigated thoroughly by Zhou *et al.,* (2013), in which they stated that they hope that this combination will be more stable than Germanene while maintaining the Dirac point at the K point of the Brillouin Zone.

3.2.1   Structural Properties

Both authors have stated that the only stable structure for siligene is low-buckled honeycomb (shown in Figure 3.3(a)) which they have confirmed by plotting phonon dispersion (see Figure 3.3(b)), which does not contain any negative frequencies mode. Zhou *et al.* (2013) also plotted the phonon dispersion for high-buckled honeycomb siligene which shows negative frequencies mode, thus proving its instability. They further investigated the stability by calculating the contribution of lattice vibration to the free energy, in which the outcome suggests siligene is stable, with the stability even higher than silicene which has been experimentally fabricated.

The structural constants of siligene from various sources are shown in Table 3.2. We notice that all the published values have very good agreement on both lattice constant and buckling distance which is about 3.94 Å and 0.58 Å, respectively, even when the XC functional used are different. Figure 3.3(a) shows the top view of LB siligene.

a)   b)
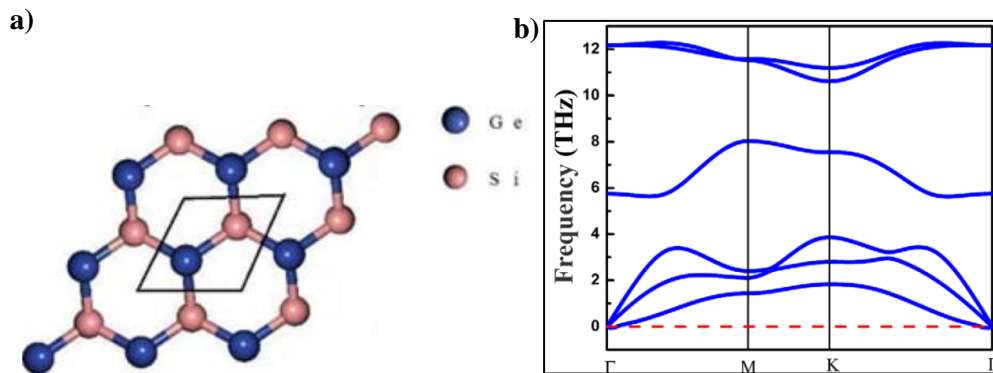
Figure 3.3: (a) Top View of LB Siligene with the Parallelogram Indicating 1×1
           Supercell (Sakib, Ahmed and Subrina., 2018). (b) Phonon
           Dispersion for Siligene (Zhou *et al.*, 2013).

Table 3.2: Structural Constants of Siligene from Multiple Sources

Sources	XC Functional	Lattice Constant, Å	Buckling Distance, Å
Pan *et al.* (2011)	LDA	3.94	0.57
Zhou *et al.* (2013)	GGA	3.939	0.579
Jamdagni *et al.* (2015)	LDA	3.95	0.57
Sakib, Ahmed and Subrina (2018)	GGA	3.94	0.59
Sannyal, Ahn, and Jang (2019)	GGA	3.91	0.58

3.2.2 Electronic Properties and Tunability

According to Pan *et al.* (2011), siligene is a band gapless semimetal with band crossings at the K point of the BZ. The findings of Zhou et al. (2013) agree with the findings of Pan *et al.* (2011) and they stated further that the band crossings at K point are linear, which resembles a Dirac cone (see Figure 3.4), thus giving both electrons and holes a massless Dirac fermion characteristics, similar to germanene. Contrary to other findings, Jamdagni *et al.* (2015) and Sakib, Ahmed and Subrina (2018) reported a small band gap of 0.15 eV and 0.6 eV respectively, while they both agree on the presence of Dirac cone at K point of the BZ. The differences are likely to be due to the different functionals or parameters used as the band gap is small and thus any delicate parameter changes could have affected the results.
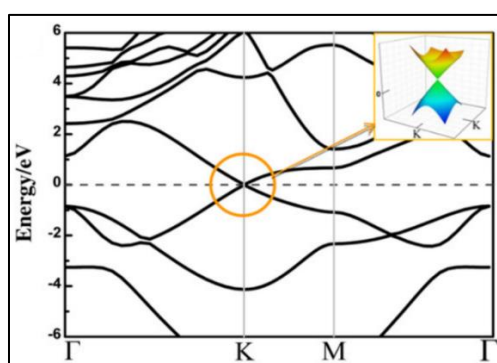
Figure 3.4: Electronic Band Structure for Siligene. Inset is Showing the 3D Dirac Cone at K point. (Zhou *et al.*, 2013).

Under both tensile and compressive uniaxial strain, the band gap of siligene has shown to increase almost linearly with deviation from linear behaviour starting at 6% strain while the mass of the charge carriers (electron and photon) only increase slightly, thus preserving the very high charge carrier mobility (Sakib, Ahmed and Subrina, 2018). For uniaxial compressive strain above 6%, siligene undergoes a direct metallic transition while for uniaxial tensile strain, the band gap of siligene transitioned from direct to indirect.

The effects of biaxial strain and vertical electric field were investigated by Jamdagni *et al.* (2015). Under biaxial tensile strain, the band gap (which was reported to be 0.15 eV by the same author) becomes smaller and smaller, eventually reaching zero at 6% strain. For biaxial compressive strain, the band gap increases somewhat parabolic-like until 6% strain at 0.55 eV, before falling to zero drastically at 8% strain. When an external vertical electric field is applied to siligene, the band gap opens up further and varies almost linearly with external electric field strength, up to about 0.80 eV when 1 V/Å electric field is applied.

The impressive tunability of siligene under both mechanical strain and electric field renders siligene a very attractive candidate for nanoelectronics and optoelectronics applications. However, siligene is yet to be synthesized experimentally.

3.3 Justification for the Choice of Monolayers

The lattice mismatch between Germanene and Siligene is low, with only about 2.2% difference. This is a good indication that the defects arise due to lattice mismatch during the crystal growth of the 2D SiGe/Ge heterostructure could be reduced as well. Moreover, both Germanene and Siligene have low-buckled honeycomb structure. This indicates that the heterostructure will be easier to grow.

Furthermore, both of the monolayers contain Dirac cone in their electronic band structure which is an indication of high charge carrier mobility. Hence, it is likely that the combined heterostructure will have Dirac cone as well which is desirable for nanoelectronics applications.

The tunability of both monolayers are attractive features as well. There is a high possibility that the heterostructure will inherit this attribute.

3.4   Band Gap Tuning using Oxygen Adsorption

By adsorbing oxygen atoms onto the surface of a monolayer graphene experimentally, Takahashi *et al*. (2014) has successfully opened a band gap of 0.45 eV in the bandgap-less graphene.

Similarly, Du *et al.* (2014) oxidized silicene, which has no band gap in its pristine form, and successfully opened a band gap of about 0.18 eV. They also note that the silicene monolayer retains its structure when fully covered by oxygen adatom.

Oxygen adsorption is a promising method to tune the electronic properties of monolayers and open band gap in a bandgap-less material, expanding the possibility of nanoelectronics applications.

CHAPTER 4

METHODOLOGY AND WORK PLAN

4.1 Computation using Quantum ESPRESSO

In this research, Quantum Espresso (QE) is employed to implement DFT calculation. The logo of QE is shown in Figure 4.1. QE is an open-source computational package where ESPRESSO is an acronym for opEn-Source Package for Research in Electronic Structure, Simulation, and Optimization. QE was first released in 2009 by Giannozzi *et al.,* and further improved the functionality in 2017. The package requires the use of a Linux-based operating system such as Ubuntu and supports parallel processing with the help of MPI package. Other than QE, there is also VASP available for DFT calculation. QE is chosen over VASP as QE is an open-source package which is also free to use.

Figure 4.1: The Logo of Quantum ESPRESSO. (Giannozi, 2009)

QE supports many different types of calculations such as SCF calculation, molecular dynamics (MD), phonon dispersion calculation, and quantum transport. The features used in this research are SCF and phonon dispersion calculation, which are separated in several subpackages, which includes Pw, Bands, Dos, Projwfc, and ph. Pw is used for geometrical optimizations and self-consistent field (SCF) calculations; Bands processes the output file of SCF calculation and produces electronic band structure; dos and Projwfc are used to obtain DOS and PDOS, respectively; Ph is used for phonon dispersion calculation within density functional perturbation theory (DFPT) framework.

4.2   Visualizing crystal structure using XCrySDen

XCrySDen is a graphical visualizer package developed by Kokalj (1999). It is used to visualize the input and output files of several DFT software such as Quantum ESPRESSO, VASP and others. Using XCrySDen, we can view the crystal structure, measure interatomic distance between any of the two atoms involved, and measure bond angle. When setting up the crystal structure for geometrical relaxation, we can use XCrySDen to help determine and verify where the position of the atoms. The user interface of XCrySDen is shown in Figure 4.2(a), while Figure 4.2(b) demonstrates how to measure bond distance.
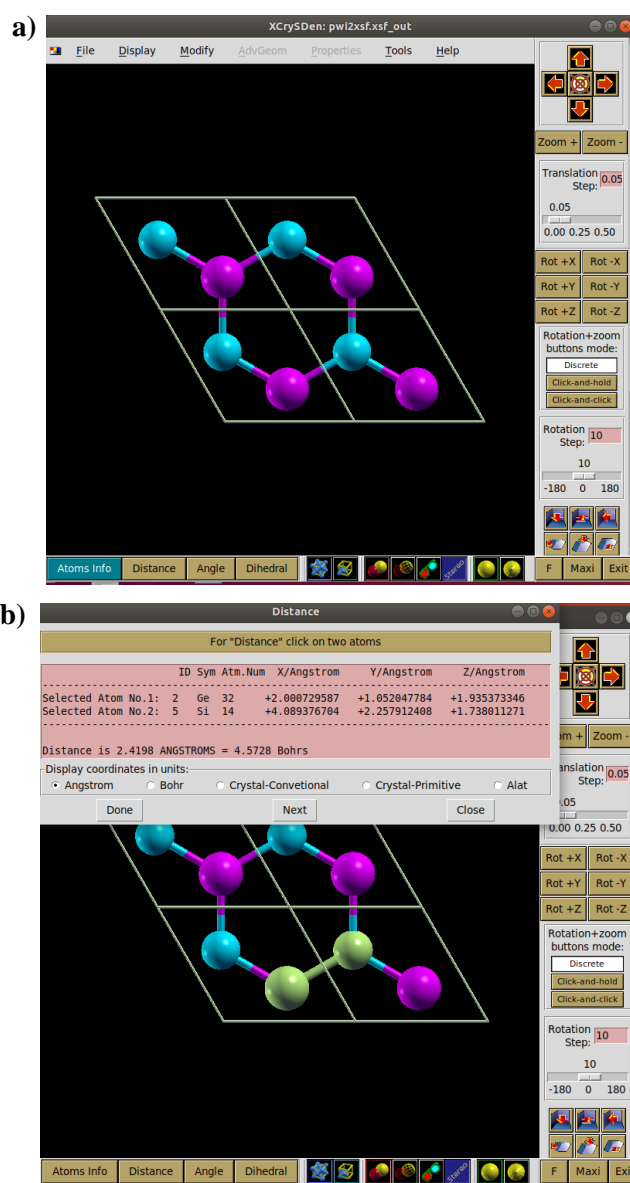
Figure 4.2: (a) User Interface of XCrySDen. (b) Example of Measuring Atomic Distance using XCrySDen.

4.3 Carrying out Calculation

To run any calculation, an input file containing various parameters is required. Figure 4.3(b) and Figure 4.3(c) shows an example of geometrical optimization and phonon input file respectively. After creating the required input file, the computation can be executed by running a command in a Linux terminal, as shown in Figure 4.3(a).

For SCF calculation, we are required to specify convergence threshold for total energy, total force, and individual SCF cycle, crystal structure such as the lattice vector and atomic positions, kinetic energy cutoff, structural optimization algorithm (for geometrical optimization), atomic species, type of van der Waals' correction, XC functional, pseudopotential, and k-grid. For the phonon dispersion calculation, the required parameters are q-grid and convergence threshold.

A typical QE calculation steps are shown in Figure 4.4.
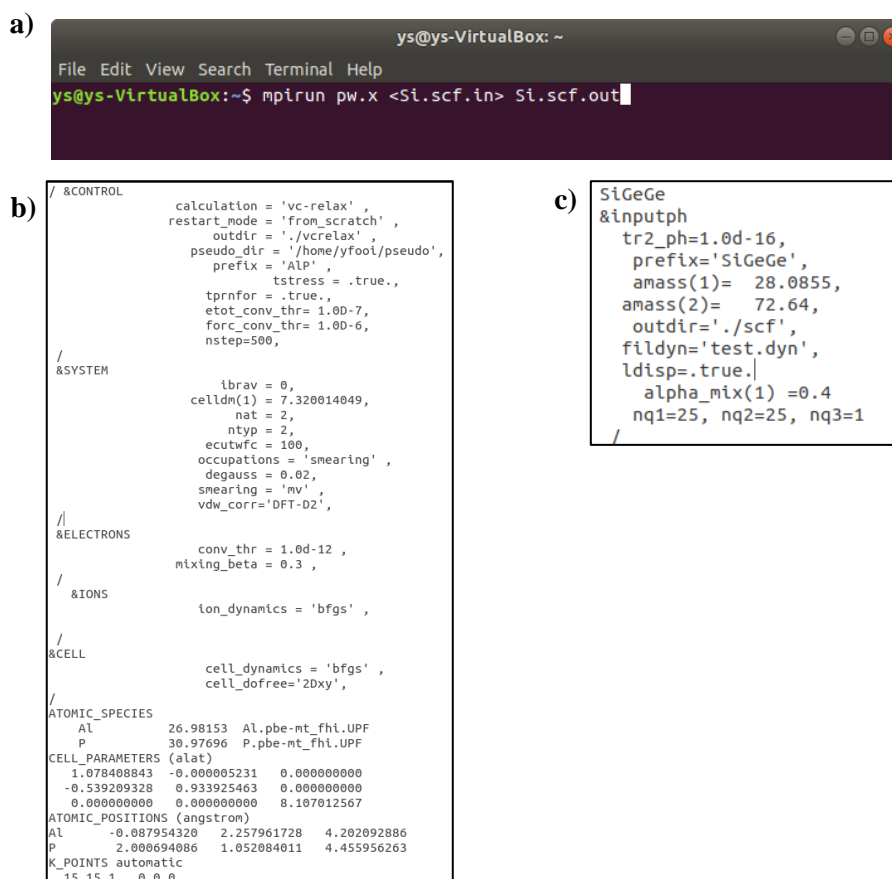
Figure 4.3: (a) Command Required to Initiate the Computation. Sample Input File for (b) Geometrical Relaxation and (c) Phonon Calculation
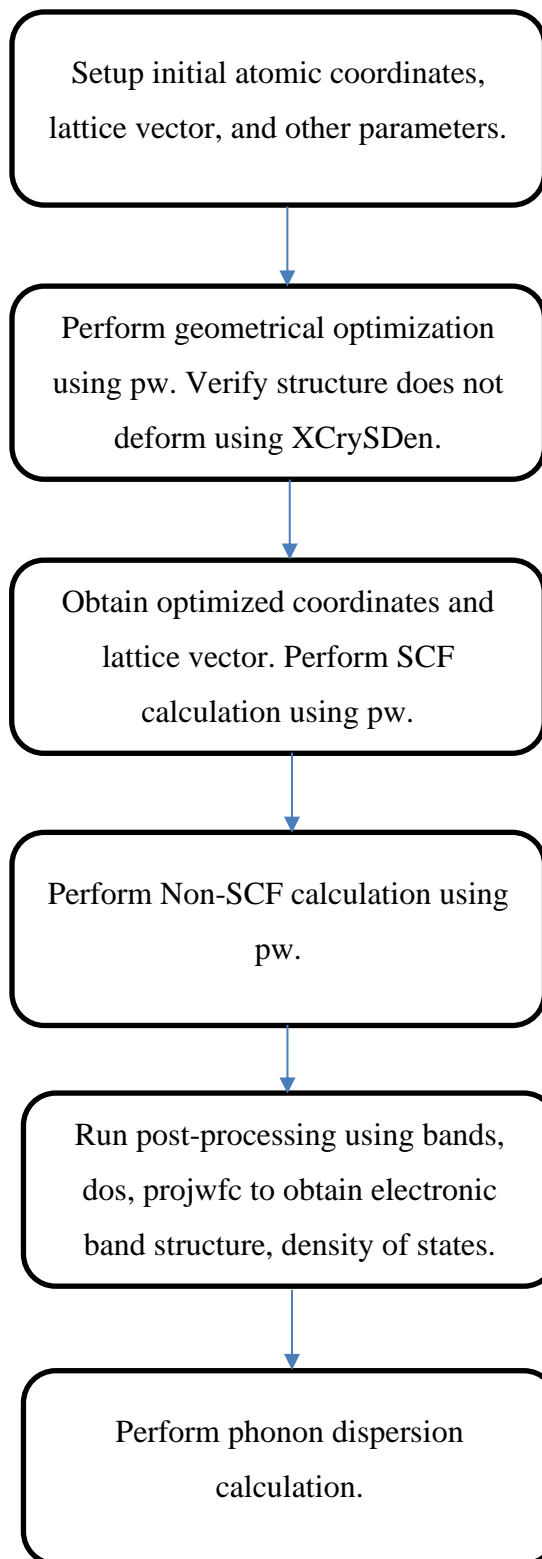
Figure 4.4: Flowchart for DFT Calculation using Quantum ESPRESSO.

4.4   XC Functional and Parameters

The XC functional used in this project is Perdew–Burke–Ernzerhof (PBE) based Generalized Gradient Approximation functional, whereas the pseudopotential employed is Troullier-Martins type norm-conserving pseudopotential. For k-points grid, Monkhorst-Pack uniform $25 \times 25 \times 1$ k-points grid is used for SCF calculation, whereas $10 \times 10 \times 1$ is used for geometrical optimization. The geometrical optimization algorithm used is the Broyden–Fletcher–Goldfarb–Shanno (BFGS) algorithm. Kinetic energy cut-off of 80 Ry is applied in all of the computations. A 20 Å vacuum is established along the perpendicular direction of the supercell to minimize any interaction between layers. The van der Waals' correction used is Grimme-D2 type. For phonon dispersion calculation, a q-grid of $8 \times 8 \times 1$ is used.

Figure 4.5 shows the Brillouin zone and high symmetry point for hexagonal lattice. For electronic band structure and phonon dispersion calculation, the high-symmetry points chosen are: Γ, K, M with path $\Gamma \rightarrow K \rightarrow M \rightarrow \Gamma$, which is the research standard for honeycomb structure.
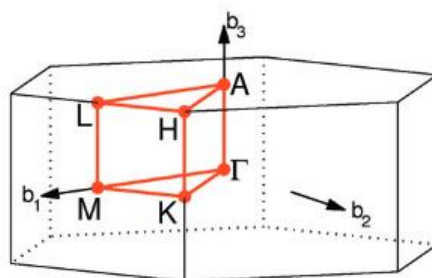
Figure 4.5: Brillouin Zone for Hexagonal Lattice. High Symmetry Points are Labelled in Red. (Setyawan and Curtarolo, 2010)

4.5 Work Plan

In this project, we aim to replicate and compare the properties for the monolayers, namely Germanene and Siligene with published literature, and investigate the structural, mechanical and electronic properties of the 2D SiGe/Ge heterostructure. To explore the heterostructure, we need the atomic coordinates of the monolayers before we can proceed with the computation. After the calculations for monolayers are completed, the work for heterostructure can begin. The work starts with the geometrical optimization of the structure, followed by electronics properties calculation and phonon dispersion calculation. Then both compressive and tensile biaxial strain to the heterostructure up to 10% are applied to the heterostructure, to probe its stress-strain response and effect of biaxial strain on its electronic properties. Finally, oxygen is adsorbed onto the surface of the heterostructure using 1×1 supercell to study the effect of oxygen adatom on the electronic properties of the heterostructure.

4.6 Work Stages

The work for this project can be divided into five main stages. The first main stage is the relaxation or geometrical optimization of the monolayers, which are siligene and germanene. This is done by first creating an input file containing initial atomic coordinates and lattice vectors along with other required parameters. A command input is then used to start the computation. During the relaxation, the atomic coordinates and lattice vectors will change iteratively depending on the force which is calculated using Hellman-Feynman theorem coded within the PW package, until convergence is reached. After that, we can execute the self-consistent field (SCF) calculation using the final coordinates from the relaxation. The SCF calculation computes the fermi energy, and outputs the raw files which can be used to generate electronic band structure and phonon dispersion calculation. We then compare our results with published literature. If there is no significant disparity, we continue to the next stage.

The second main stage is the combination of the two monolayers. The final relaxed coordinates of the two monolayers are combined with the help of XCrySDen. Then, geometrical optimization is done to obtain the optimized

structure. SCF calculation is the next step, which outputs data that we can extract the electronic band diagram and density of states from.

The third main stage is the phonon dispersion calculation, which is the most time-consuming task. An input file along with the iterative convergence parameters are included along with the density of the q grid. These 2 parameters will directly affect the computational time. After the calculation is completed, the raw data are extracted for graph plotting and analysis.

The fourth main stage is the tuning of the electronic properties by the use of biaxial tensile and compressive strain, and oxygen adsorption. After the computations are done, we can extract the electronic band structures and analyse the effect of biaxial strain and oxygen adsorption. The stress-strain curve of the heterostructure can also be collected from the output data of biaxial strain calculation.

The last stage is graph plotting and analysis of the data collected. Electronic band structure, DOS, and phonon dispersion are plotted by using Origin 2015, a professional graph plotting software. The graphs are then analysed thoroughly to identify the mechanical and electronic properties of the heterostructure.

CHAPTER 5

RESULTS AND DISCUSSION

5.1   Germanene

5.1.1   Structural Properties

The only stable structure for Germanene is low-buckled honeycomb (shown in Figure 5.1), as discussed in section 3.1.1, thus other structures are not considered in this study.
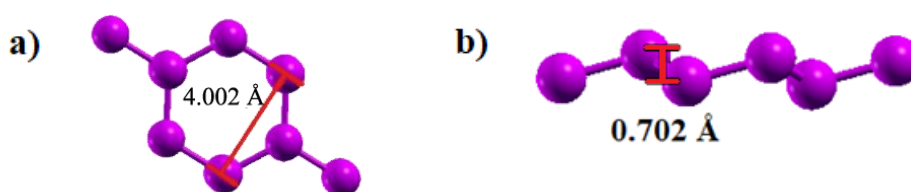
Figure 5.1: (a) Top and (b) Side View of The Germanene Monolayer in a 2×2 Supercell from XCrySDen. The Red Lines Denotes (a) Lattice Constant and (b) Buckling Distance

The lattice constant and buckling distance of this study is tabulated in Table 5.1 along with other published results using the same functional, which is GGA. From Table 5.1, we can see that the lattice constant agrees closely with published results, especially with Ni *et al*. (2012). If we include the results that used GGA (from Table 3.1), we see that the value reported here is in between the LDA and GGA studies. The buckling distance is slightly higher than the value published by Ni *et al.* (2012), with only a small difference of 0.026 Å.

Table 5.1: Structural Constants of Germanene Compared with Publication Using Same GGA Functional.

Sources	Lattice Constant, Å	Buckling Distance, Å
Lebègue and Eriksson (2009)	4.126	(Not included)
Ni *et al.* (2012)	4.063	0.676
This study	4.002	0.702

5.1.2 Electronic Properties

The electronic band structure plotted in Figure 5.2 is in agreement with the published result from Cahangirov *et al.* (2009) shown in Figure 5.2(b). Band gap is absence from the electronic band structure and a Dirac cone is present at the K point of the Brillouin zone.
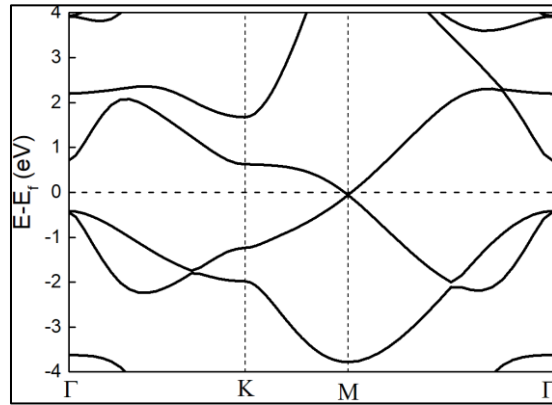
Figure 5.2: Electronic Band Structure for Germanene from This Study.

5.2   Siligene

5.2.1   Structural Properties

As reported, siligene has a stable low-buckled honeycomb structure (shown in Figure 5.3). In this study, low-buckled honeycomb siligene is studied and the findings for structural properties are compared with published results mentioned in section 3.2.1. The results are tabulated together in Table 5.2. As can be observed from Table 5.2, the calculated lattice constant and buckling distance are both in good agreement with previous calculations that employed GGA functional.
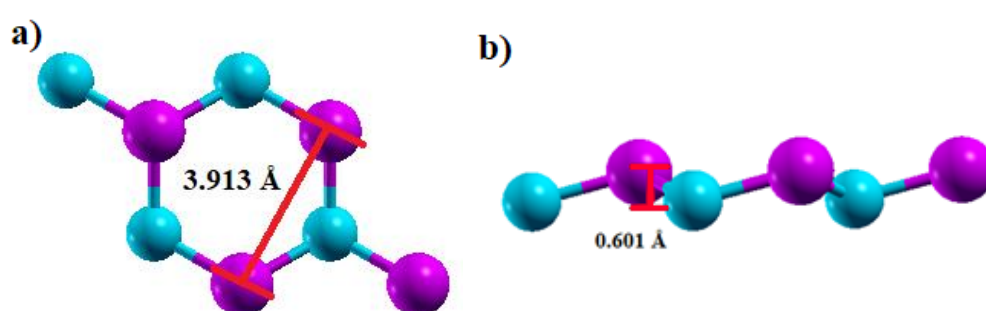
Figure 5.3: (a) Top and (b) Side View of Siligene in a 2×2 Supercell from XCrySDen. The Red Lines Denotes (a) Lattice Constant and (b) Buckling Distance

Table 5.2: Structural Constants of Siligene along with Published Results Using GGA Functional.

Sources	Lattice Constant, Å	Buckling Distance, Å
Zhou *et al.* (2013)	3.939	0.579
Sakib, Ahmed and Subrina (2018)	3.94	0.59
Sannyal, Ahn, and Jang (2019)	3.91	0.58
This study	3.913	0.601

5.2.2 Electronic Properties

The electronic band structure for siligene is plotted in Figure 5.4, which agrees closely with the published result (see Figure 3.4). The band structure shows a linear dispersion or Dirac cone at K Point of the Brillouin Zone. From the band structure, it is clear that siligene is bandgapless. Thus, the results agree with Pan *et al.* (2011) and Zhou *et al.* (2013) which mentioned that band gap is absent in siligene, while disagreeing with Jamdagni *et al.* (2015) and Sakib, Ahmed and Subrina (2018), which reported a band gap of 0.15 eV and 0.6 eV respectively.
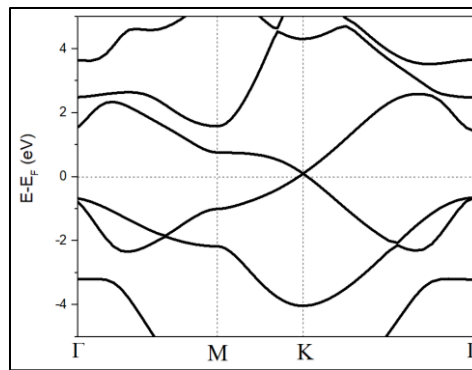
Figure 5.4: Electronic Band Structure for Siligene from This Study

5.3   Siligene-Germanene Heterostructure

Germanene and siligene have very similar low-buckled structure, including their lattice constants and buckled distance, with a small difference of 0.1 Å in both cases. Thus, stacking them up is straightforward, which yields 10 possible combinations, which are then known as Siligene-Germanene Heterostructure or in short 2D SiGe/Ge. There are two main different types of stacking, which are AA and AB stacking. They are shown in Figure 5.5. Among AA stacking, there are 4 different ways of stacking, whereas for AB stacking there are 6 different ways, because of the buckled structure of both germanene and siligene.

After geometrical optimization, all AA structures have changed into the same planar AA structure, whereas all AB structures have deformed except the structure shown in Figure 5.5(d)(vi). From this section onwards, the two structures will be named as AA structure and AB structure respectively.

a) AA stacking   **b) AB stacking**

i)   ii)   i)   ii)

c) Possible AA stacking

i)   ii)   iii)   iv)

d) Possible AB stacking

i)   ii)   iii)   iv)   v)   vi)
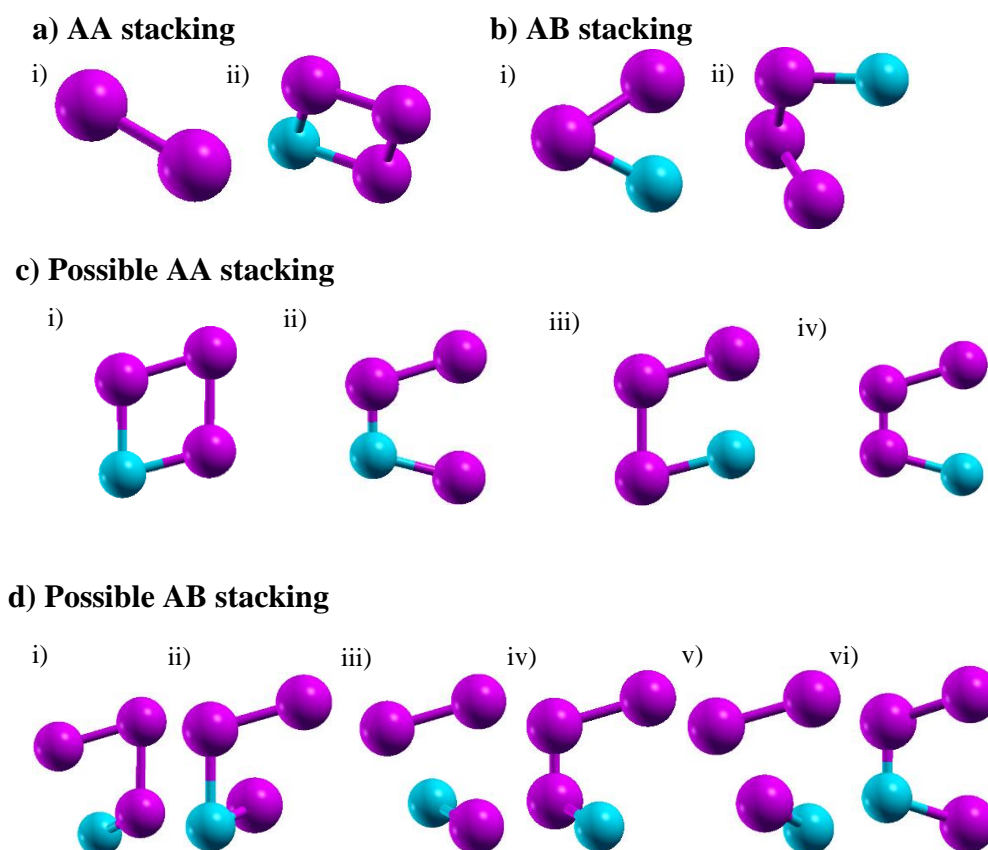
Figure 5.5: 1×1 Supercell of (a) AA Stacked 2D SiGe/Ge Heterostructure and (b) AB stacking with (i) Top View and (ii) Tilted View. (c) (i-iv) Side View of Four Different AA Stacking. d) (i-vi) Side View of Six Different AB Stacking.

5.3.1 Structural Properties

The structural constants of both AA and AB structure are tabulated in Table 5.3. Figure 5.6 shows the planar AA structure and buckled AB structure from different views. The AA structure has a large lattice constant compared to the constituent monolayers (siligene and germanene), whereas for the AB structure, the lattice constant is in situated between the value of the two monolayers.

From the buckling distance, we can observe that the AA structure is planar, as the buckling distance is negligible, which is in contrast with both of the monolayers; AB structure has a low-buckled (LB) structure. The buckling distance of AB structure is larger than the two monolayers, which are 0.7015 and 0.6005 Å, respectively for germanene and siligene.

Table 5.3: Structural Constants of the 2D SiGe/Ge Heterostructures.

Structure	Lattice Constant / Å	Buckling Distance (Ge-Ge) / Å	Buckling Distance (Si-Ge) / Å	Formation energy per atom / eV
AA	4.302	0.031	0.053	-0.184
AB	3.934	0.873	0.699	-0.167

a) AA structure
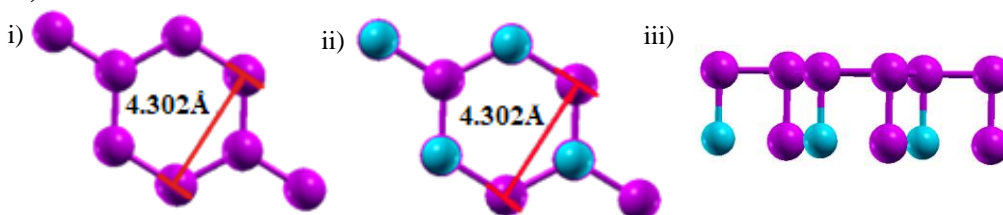
b) AB structure
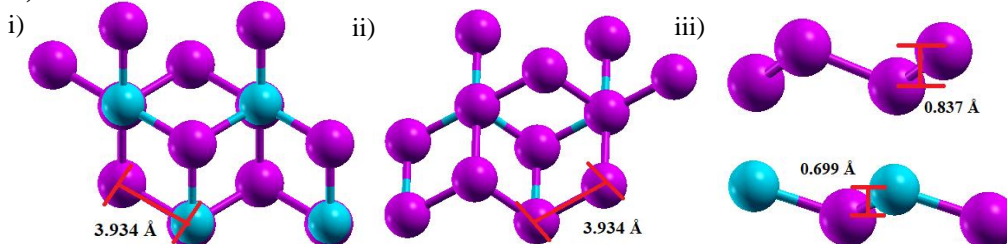
Figure 5.6: (i) Top view from Germanene side, (ii) Top View from Siligene, and (iii) Side View for Optimized (a) Planar AA Structure and (b) Buckled AB Structure.

The formation energy per atom, represented by E_{form}, is calculated by using the formula below:

$$E_{form} = \frac{E_{total}(Heterostructure) - E_{total}(Germanene) - E_{total}(Siligene)}{no.\,of\,atoms} \quad (5.1)$$

where E_{total} is the total energy of the structure obtained from the output of SCF calculation and number of atoms equals to 4 for this study because a 1×1 supercell contains 4 atoms. Negative formation energy indicates the structure is energetically favourable, while the larger the magnitude indicates better cohesion of the structure. From Table 5.3, the formation energy per atom of the AA structure is larger in magnitude when compared to the AB structure, which indicates a better cohesion for the AA structure comparatively.

The phonon dispersion for both AA and AB structure are shown in Figure 5.7. The phonon dispersion for the AB structure displays a negative frequency of about 16 cm^{-1} at Γ point, which is a sign of dynamical instability. While the AA structure also have negative frequency with the maximum negative frequency being 5 cm^{-1}. However, the negative frequency does not occur at Γ point, but at other points not included in the calculation, which are interpolated instead. Calculating the phonon dispersion at the particular interpolated points reveal that those points are positive (displayed as black square in the Figure 5.7a), and the phonon dispersion does not contain any negative frequency, indicating the structure is dynamically stable. As the AB structure is unstable, no further discussion on the structure will be made.
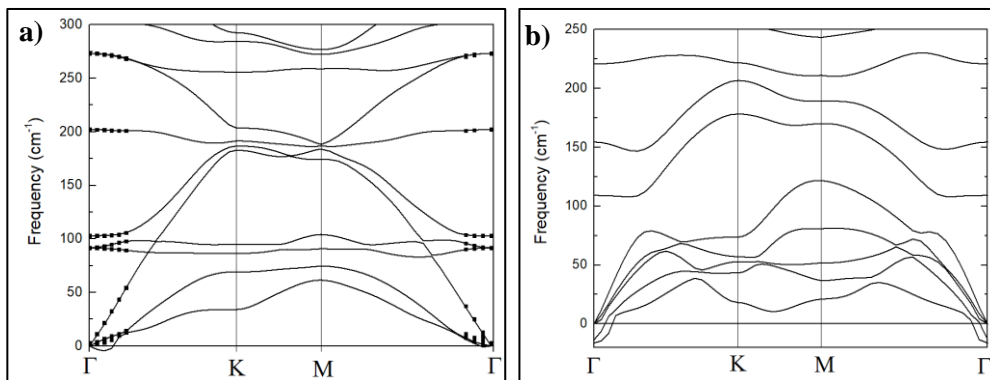
Figure 5.7: Phonon Dispersion for (a) AA Structure (Black Square Indicates Corrected Value) and (b) AB Structure.

5.3.2   Mechanical Properties

Figure 5.8 shows the stress-strain characteristic of the heterostructure obtained by applying biaxial strain to the heterostructure. Negative strain means compressive strain while positive strain implies tensile strain. In the stress-strain curve, we can observe an almost linear trend with a negative slope from -4% to 6% strain. The trend is discontinued at both -6% strain and 8% strain, where the slopes change sign. This indicates that the heterostructure has started to display mechanical fracturing. The ultimate tensile strength for the heterostructure is about 18 kbar or 1.8 GPa.
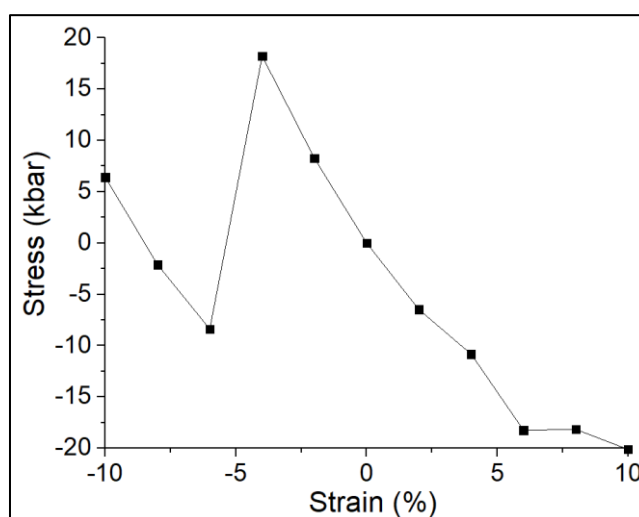
Figure 5.8: Stress-Strain Curve for 2D SiGe/Ge Heterostructure when Biaxial
Strain is Applied.

5.3.3   Electronic Properties

The electronic band structure of the heterostructure along with the DOS and partial DOS (PDOS) are plotted in Figure 5.9. The Fermi level indicates that the heterostructure has a metallic characteristic. This is further confirmed by the DOS, where at the Fermi level, there are comparatively substantial amount of electronic states.

In both of the monolayers, there is a gaped Dirac cone at the K point. In the heterostructure, the Dirac cone remains at the K point but is situated below the Fermi level. Further attempt to tune the electronic properties and shift the tip of the Dirac cone to the Fermi level could result in a high carrier mobility.

The PDOS shows the contribution of p orbital of each atom in the unit cell towards the electronic state, wherein the plot indicates an equal amount of contribution from each atom, which is likely due to the similarity in the composition between germanene and siligene with silicon and germanium having only a small difference in electronegativity. Note that the value plotted for the PDOS are multiplied by two for better clarity, as their magnitudes are low in comparison with the total DOS. The s orbitals are omitted due to their negligible contribution to electronic states.
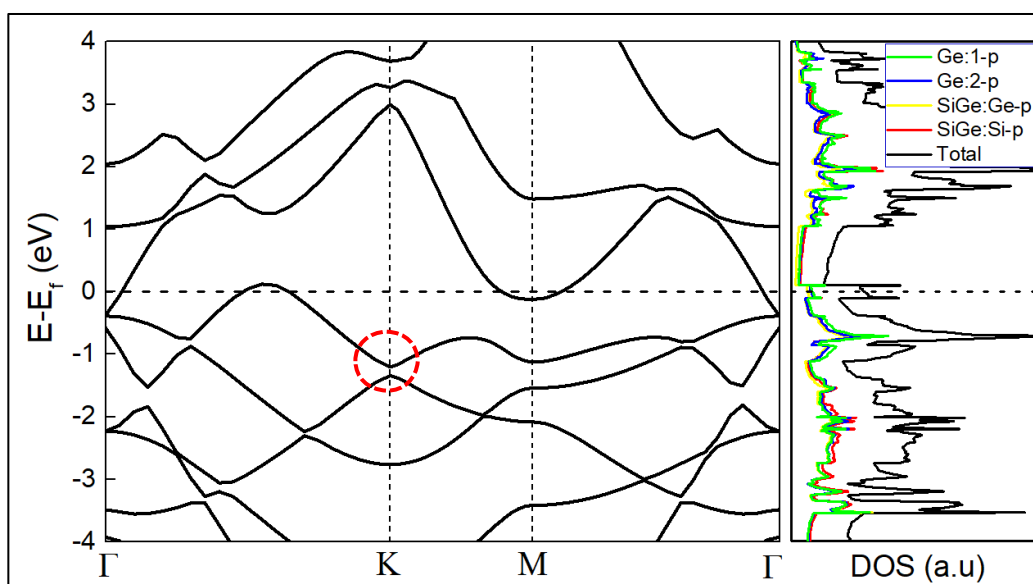
Figure 5.9: Electronic Band Structure with DOS for the Heterostructure. The Dirac Point is Circled in Red.

5.3.4   Effects of Biaxial Strain

The effects of both compressive and tensile biaxial strain on electronic band structure are shown in Figure 5.10 and 5.11 respectively, where the effect of up to 4% compressive strain and 6% for tensile strain are shown.

For tensile strain, we can observe the two lobes near K and M points are shrinking vertically, while the Fermi level shifts downward. The heterostructure eventually converts from metallic to semimetallic at 6% tensile strain. It is worth noting that a tiny band gap may have been opened for the heterostructure at 6% tensile strain. A DOS has been plotted to verify the existence of said band gap. Unfortunately, a small but non-negligible amount of electronic states exist which signifies a semimetallic behaviour.

Under compressive strain, a gap at the Γ point is slowly opening but the two lobes remain unchanged. At 4% compressive strain, a gap has been fully opened at Γ point. However, the Fermi level still lies across the two lobes which implies metallic behaviour.
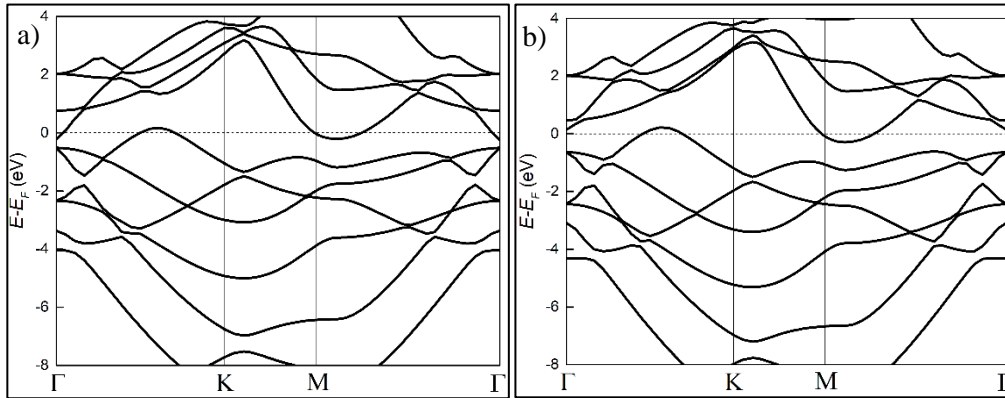
Figure 5.10: Electronic Band Structure for Compressive Strain: (a) 2% and (b) 4% .
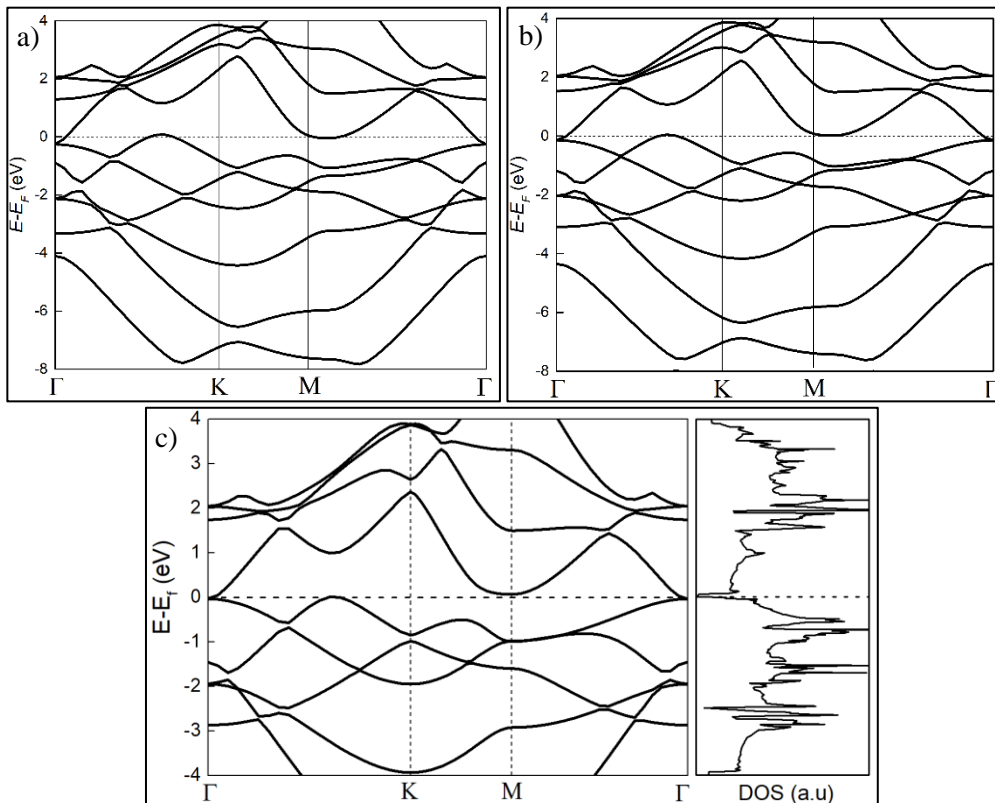
Figure 5.11: Electronic Band Structure for Tensile Strain: (a) 2%, (b) 4%, and (c) 6%. DOS is Attached for 6% Tensile Strain.

5.3.5   Oxygen Adatom Functionalization

In an attempt to open a band gap, oxygen adsorption has been explored. There are 8 possible adsorption sites that have different environment as shown and labelled numerically in Figure 5.12(a) and Figure 5.12(b). After geometrical optimization, only position 2,3, 6 and 7 are not deformed. For position 2 and 6, the planar heterostructure becomes buckled, while for position 6 and 7, the heterostructure remains planar. The most energetically favourable configuration is position 7 (shown in Figure 5.12(c)), thus it is the only selected configuration for subsequent calculation.

The electronic band structure and DOS of the selected configuration is plotted in Figure 5.12(d). From the plot, we notice that a band gap has been opened which lies at the gamma point. The band gap obtained from the DOS is about 0.24 eV. The opening of band gap of the heterostructure gives rise to possible nanoelectronics applications.
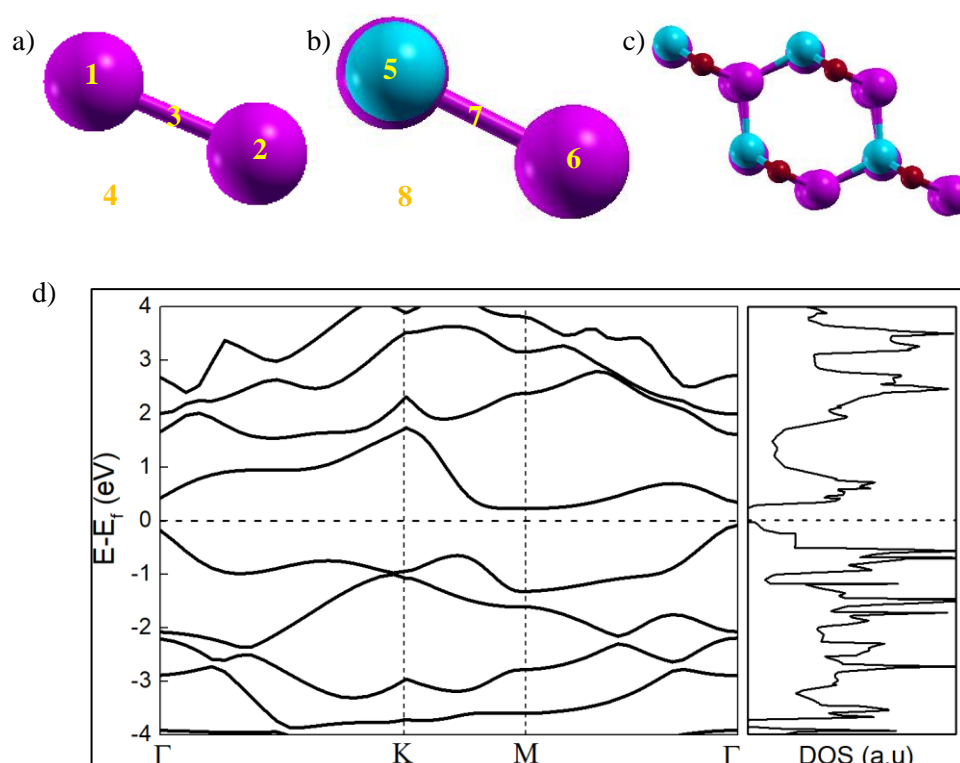
Figure 5.12: Possible Adsorption site for 2D SiGe/Ge Heterostructure shown on a 1×1 Supercell, where (a) is the Top View from Germanene and (b) Siligene of the Heterostructure. The Side View of the 2×2 Selected Configuration is Displayed in (c). The Electronic Band Structure and DOS for the Selected Configuration is Plotted in (d).

CHAPTER 6

CONCLUSIONS AND RECOMMENDATIONS

6.1   Conclusions

In this study, the density functional theory has been employed by using Quantum ESPRESSO package to replicate and compare the results of monolayer Ge (germanene) and monolayer SiGe (siligene), and to predict and study the 2D SiGe/Ge heterostructure by combining germanene and siligene, with a focus on the structural, mechanical, and electronic properties. The structural and electronic properties of germanene and siligene are in good agreement with previous studies. Germanene and siligene both have a low-buckled (LB) honeycomb structure with semimetallic characteristics and contain a Dirac cone at the K point of BZ.

It was found that there are 10 possible different ways to stack siligene and germanene together, but only 2 of them do not deform after geometrical optimization. After plotting phonon dispersion, it was revealed that only one of them is dynamically stable. The stable structure is AA-stacked with a planar honeycomb structure.

By plotting electronic band structure and DOS, it was revealed that the heterostructure has metallic characteristic. The heterostructure has ultimate strength of about 18 GPa and starts to breakdown after 6% biaxial tensile strain or 4% biaxial compressive strain.

The effect of biaxial strain on the electronic properties of the heterostructure was studied. A shift from metallic to semimetallic characteristic under 4% or more compressive strain were revealed. The electronic band structure was also tuned by adsorbing oxygen atoms onto the surface of the heterostructure, which successfully opened a band gap of 0.24 eV.

This metallic heterostructure may be a promising upcoming material for applications such as battery anode and IC interconnects. The band gap opening of the heterostructure when oxygen is adsorbed may also open up possibilities of nanoelectronics application.

6.2   Recommendations for future work

In our study of oxygen adatom, the computation was carried out on a 1×1 supercell which is inadequate. To address this problem, a larger supercell of 3×3 needs to be used which drastically increases the computation time and computational resources needed, which are limited as mentioned previously. Adatoms other than oxygen should be explored which are again not permitted by the limitations.

Extensions to this work that can be done include the study of the effect of vertical electric field on the electronic band structure to find an alternative method to open a band gap. This is a promising method as shown by both Jamdagni *et al.* (2015) and Ni *et al.* (2012), where they have successfully opened a band gap in siligene and germanene, respectively. The opened band gap magnitude also varies almost linearly with the electric field strength for both materials.

Further extensions to explore the application of the heterostructure such as battery anode and gas sensing application will be interesting as well. The result from Sannyal, Ahn, and Jang (2019) suggests siligene to be a good candidate as an anode material of an alkali metal ion battery, with high theoretical charging capabilities and good voltage profiles. A very recent publication by Sun *et al.* (2020) explored the gas sensing capabilities of siligene using DFT. The result indicates that the siligene has good gas sensing capabilities especially for NO_2 and NH_3 gases. The heterostructure may inherit the same properties from the monolayers or have an even better performance.

REFERENCES

Akbari, E., Jahanbin, K., Afroozeh, A., Yupapin, P. and Buntat, Z., 2018. Brief review of monolayer molybdenum disulfide application in gas sensor. *Physica B: Condensed Matter*, *545*, pp.510-518.

Akinwande, D., Brennan, C., Bunch, J., Egberts, P., Felts, J., Gao, H., Huang, R., Kim, J., Li, T., Li, Y., Liechti, K., Lu, N., Park, H., Reed, E., Wang, P., Yakobson, B., Zhang, T., Zhang, Y., Zhou, Y. and Zhu, Y., 2017. A review on mechanics and mechanical properties of 2D materials—Graphene and beyond. *Extreme Mechanics Letters*, 13, pp.42-77.

Akinwande, D., Huyghebaert, C., Wang, C.H., Serna, M.I., Goossens, S., Li, L.J., Wong, H.S.P. and Koppens, F.H., 2019. Graphene and two-dimensional materials for silicon technology. Nature, 573(7775), pp.507-518.

Butler, S., Hollen, S., Cao, L., Cui, Y., Gupta, J., Gutierrez, H., Heinz, T., Hong, S., Huang, J., Ismach, A., Johnston-Halperin, E., Kuno, M., Plashnitsa, V., Robinson, R., Ruoff, R., Salahuddin, S., Shan, J., Shi, L., Spencer, M., Terrones, M., Windl, W. and Goldberger, J., 2013. Progress, Challenges, and Opportunities in Two-Dimensional Materials Beyond Graphene. *ACS Nano 2013 7 (4), 2898-2926*.

Cahangirov, S., Topsakal, M., Aktürk, E., Şahin, H. and Ciraci, S., 2009. Two- and one-dimensional honeycomb structures of silicon and germanium. *Physical review letters*, *102*(23), p.236804.

Dai, Z., Liu, L. and Zhang, Z., 2019. Strain Engineering of 2D Materials: Issues and Opportunities at the Interface. *Advanced Materials*, p.1805417.

Dávila, M.E., Xian, L., Cahangirov, S., Rubio, A. and Le Lay, G., 2014. Germanene: a novel two-dimensional germanium allotrope akin to graphene and silicene. *New Journal of Physics*, *16*(9), p.095002.

Du, Y., Zhuang, J., Liu, H., Xu, X., Eilers, S., Wu, K., Cheng, P., Zhao, J., Pi, X., See, K.W. and Peleckis, G., 2014. Tuning the band gap in silicene by oxidation. *ACS nano*, *8*(10), pp.10019-10025.

Garay-Tapia, A., Romero, A. and Barone, V., 2012. Lithium Adsorption on Graphene: From Isolated Adatoms to Metallic Sheets. *Journal of Chemical Theory and Computation*, 8(3), pp.1064-1071.

Geim, A.K. and Grigorieva, I.V., 2013. 'Van der Waals heterostructures', *Nature*, 499(7459), pp. 419–425.

Giannozzi, P., Andreussi, O., Brumme, T., Bunau, O., Nardelli, M.B., Calandra, M., Car, R., Cavazzoni, C., Ceresoli, D., Cococcioni, M. and Colonna, N., 2017. Advanced capabilities for materials modelling with Quantum ESPRESSO. *Journal of Physics: Condensed Matter*, 29(46), p.465901.

Giannozzi, P., Baroni, S., Bonini, N., Calandra, M., Car, R., Cavazzoni, C., Ceresoli, D., Chiarotti, G.L., Cococcioni, M., Dabo, I. and Dal Corso, A., 2009. QUANTUM ESPRESSO: a modular and open-source software project for quantum simulations of materials. *Journal of physics: Condensed matter*, 21(39), p.395502.

Graphene, n.d. photograph, viewed 23 March 2020, https://analyticalscience.wiley.com/do/10.1002/gitlab.15487/full/#media-1

Harrison, N.M., 2003. An introduction to density functional theory. *Nato Science Series Sub Series III Computer and Systems Sciences*, *187*, pp.45-70.

Houssa, M., Pourtois, G., Afanas' Ev, V.V. and Stesmans, A., 2010. Electronic properties of two-dimensional hexagonal germanium. *Applied Physics Letters*, *96*(8), p.082111.

Jamdagni, P., Kumar, A., Thakur, A., Pandey, R. and Ahluwalia, P.K., 2015. Stability and electronic properties of SiGe-based 2D layered structures. *Materials Research Express*, *2*(1), p.016301.

Kohanoff, J., 2006. *Electronic structure calculations for solids and molecules. Theory and computational methods.* Cambridge: Cambridge University Press.

Kokalj, A., 1999. XCrySDen—a new program for displaying crystalline structures and electron densities. *Journal of Molecular Graphics and Modelling*, 17(3-4), pp.176-179.

Kuzum, D., Takano, H., Shim, E., Reed, J., Juul, H., Richardson, A., de Vries, J., Bink, H., Dichter, M., Lucas, T., Coulter, D., Cubukcu, E. and Li tt, B., 2014. Transparent and flexible low noise graphene electrodes for simultaneous electrophysiology and neuroimaging. *Nature Communications*, 5(1).

Lebègue, S., and Eriksson, O., 2009. Electronic structure of two-dimensional crystals from ab initio theory. *Physical Review B,* 79 (11), 177.

Lee, J.G., 2016. *Computational Materials Science: An Introduction*. 2nd ed. Florida: CRC Press.

Li, L., Yu, Y., Ye, G., Ge, Q., Ou, X., Wu, H., Feng, D., Chen, X.H., and Zhang, Y., 2014. Black phosphorus field-effect transistors *Nature Nanotechnology* volume 9, pages 372–377 (2014)

Liu, G., Ahsan, S., Khitun, A., Lake, R. and Balandin, A., 2013. Graphene-based non-Boolean logic circuits. *Journal of Applied Physics*, 114(15), p.154310.

Novoselov, K., 2004. Electric Field Effect in Atomically Thin Carbon Films. *Science*, 3065696, pp.666-669.

Novoselov, K., Fal′ko, V., Colombo, L., Gellert, P., Schwab, M. and Kim, K. 2012., A roadmap for graphene. *Nature*, 490(7419), pp.192-200.

Novoselov, K.S., Jiang, D., Schedin, F., Booth, T.J., Khotkevich, V.V., Morozov, S.V. and Geim, A.K., 2005. Two-dimensional atomic crystals. *Proceedings of the National Academy of Sciences*, *102*(30), pp.10451-10453.

Pan, L., Liu, H.J., Wen, Y.W., Tan, X.J., Lv, H.Y., Shi, J. and Tang, X.F., 2011. First-principles study of monolayer and bilayer honeycomb structures of group-IV elements and their binary compounds. *Physics Letters A*, *375*(3), pp.614-619.

Ponomarenko, L.A., Geim, A.K., Zhukov, A.A., Jalil, R., Morozov, S.V., Novoselov, K.S., Grigorieva, I.V., Hill, E.H., Cheianov, V.V., Fal'Ko, V.I. and Watanabe, K., 2011. Tunable metal–insulator transition in double-layer graphene heterostructures. *Nature Physics*, *7*(12), pp.958-961

Quhe, R., Fei, R., Liu, Q., Zheng, J., Li, H., Xu, C., Ni, Z., Wang, Y., Yu, D., Gao, Z. and Lu, J., 2012. Tunable and sizable band gap in silicene by surface adsorption. *Scientific reports*, *2*, p.853.

Roldán, R., Castellanos-Gomez, A., Cappelluti, E. and Guinea, F., 2015. Strain engineering in semiconducting two-dimensional crystals. *Journal of Physics: Condensed Matter*, 27(31), p.313201.

Şahin, H., Cahangirov, S., Topsakal, M., Bekaroglu, E., Akturk, E., Senger, R.T. and Ciraci, S., 2009. Monolayer honeycomb structures of group-IV elements and III-V binary compounds: First-principles calculations. *Physical Review B*, *80*(15), p.155453.

Sakib, H., Ahmed, T. and Subrina, S., 2018. "Uniaxial Strain on Monolayer SiGe: Strain Tunable Electronic Properties," *2018 10th International Conference on Electrical and Computer Engineering (ICECE)*, Dhaka, Bangladesh, 2018, pp. 313-316

Sannyal, A., Ahn, Y. and Jang, J., 2019. 'First-principles study on the two-dimensional siligene (2D SiGe) as an anode material of an alkali metal ion battery', Computational Materials Science, 165, pp. 121–128.

Setyawan, W. and Curtarolo, S., 2010. High-throughput electronic band structure calculations: Challenges and tools. *Computational materials science*, *49*(2), pp.299-312.

Sholl, D., and Steckel, J., 2009. *Density functional theory: A practical introduction*. New Jersey: John Wiley & Sons.

Song, X., Hu, J. and Zeng, H. 2013. Two-dimensional semiconductors: recent progress and future perspectives. *J. Mater. Chem. C, 2013,1, 2952-2969.*

Sun, X., Guo, Y., Zhao, Y., Liu, S. and Li, H., 2020. Gas Adsorption Investigation on SiGe Monolayer: A First-Principle Calculation. *Sensors*, *20*(10), p.2879.

Takahashi, T., Sugawara, K., Noguchi, E., Sato, T. and Takahashi, T., 2014. Band-gap tuning of monolayer graphene by oxygen adsorption. *Carbon*, *73*, pp.141-145.

Takeda, and Shiraishi, 1994. Theoretical possibility of stage corrugation in Si and Ge analogs of graphite. *Physical review. B, Condensed matter,* 50 (20), 14916–14922.

Yan, J.A., Gao, S.P., Stein, R. and Coard, G., 2015. Tuning the electronic structure of silicene and germanene by biaxial strain and electric field. *Physical Review B,* 91(24), p.245403.

Zhang, D., Akatyeva, E. and Dumitrica, T., 2011. Bending Ultrathin Graphene at the Margins of Continuum Mechanics. *Phys. Rev. Lett. 106, 255503*.

Zhang, H., Chhowalla, M. and Liu, Z., 2018. 2D nanomaterials: graphene and transition metal dichalcogenides. *Chemical Society Reviews*, 47(9), pp.3015-3017.

Zhou, H., Zhao, M., Zhang, X., Dong, W., Wang, X., Bu, H. and Wang, A., 2013. First-principles prediction of a new Dirac-fermion material: silicon germanide monolayer. *Journal of Physics: Condensed Matter*, *25*(39), p.395501.

Zhu, S. and Li, T., 2014. Hydrogenation-Assisted Graphene Origami and Its Application in Programmable Molecular Mass Uptake, Storage, and Release. *ACS Nano*, 8(3), pp.2864-2872